Biomimetic Interfaces for High-Performance Optics in the Deep-UV Light Range

Theobald Lohmüller,[†] Michael Helgert,[‡] Michael Sundermann,[§] Robert Brunner,[‡] and Joachim P. Spatz*,[†]

Max Planck Institute for Metals Research, Department of New Materials and Biosystems & University of Heidelberg, Department of Biophysical Chemistry, Heisenbergstrasse 3, D-70569 Stuttgart, Germany, Carl Zeiss AG, Technology Center, Carl-Zeiss-Promenade 10, D-07745 Jena, Germany, and Carl Zeiss AG, Technology Center, Carl-Zeiss-Strasse 56, D-73447 Oberkochen, Germany

ABSTRACT

We report an innovative approach for the fabrication of highly light transmissive, antireflective optical interfaces. This is possible due to the discovery that metallic nanoparticles may be used as a lithographic mask to etch nonstraightforward structures into fused silica, which results in a quasihexagonal pattern of hollow, pillar-like protuberances. The far reaching optical performance of these structures is demonstrated by reflection and transmission measurements at oblique angles of incidence over a broad spectral region ranging from deep-ultraviolet to infrared light.

Future communication and miniaturization systems demand the development of more efficient projection optical devices for next-generation technological breakthroughs. Today, antireflection coatings are commonly used to suppress reflection of light from the surface of optical components but also to reduce the essential transmission of light. Despite the technical importance,[1] actual material solutions for improved performance are limited, especially in the ultraviolet spectral region.[2] Today antireflection (AR) coatings are most frequently based on single- or multilayer interference structures with alternating high and low refractive indices.[3–5] An alternative to these multilayer films are subwavelength structured antireflective surfaces that provide a graded transition between the refractive indices of the two interfacing media.[6,7] Nature provides solutions for such antireflective structures (ARS) as they are found, e.g., on the corneal surfaces of a moth eye and night-active butterflies.[8,9]

Several characteristics of surfaces tailored with ARS offer distinct advantages compared to layers of thin dielectric films.[1] First, thin-film coatings suffer from mechanical stability problems like layer ablation and tensile stress if optical devices are used over a broad thermal range.[1,2] Second, appropriate coating materials with suitable refractive indices do barely exist. Common single- and multilayer configurations are therefore only applicable within a small wavelength range and normal incidence of light. In contrast, materials with ARS show a reduced and angle-independent reflectance over a broad spectral bandwidth.[10] Hybrid configurations like porous sol−gel[11] and optical polymer thin film coatings[4,12] with a nanostructured surface topology were developed to enable broadband antireflection properties. Polymer materials, however, suffer from strong absorbance and radiation damage if they are used with ultraviolet (UV) light.

Different techniques such as electron-beam writing,[13–15] mask lithography,[16] and interference lithography[17,18] have been applied to realize masters for ARS. To avoid scattering from the optical interface, the structural dimension at an optical interface has to be smaller than the wavelength of the incoming light ("lower wavelength limit").[7] For UV and DUV applications, very small feature sizes below 200 nm are therefore necessary. In this size range, conventional fabrication technologies suffer from being time-consuming, expensive, and restricted to small areas. Moreover, processing of nonplanar substrates like lenses, especially with a small radius of curvature, is hardly possible. Self-assembly based methods include techniques combining porous alumina membranes[19] or the self-organization of block copolymers with additional dry-etching.[20–22] With the latter one, the etch

---

* Corresponding author. E-mail: spatz@mf.mpg.de.
† Max Planck Institute for Metals Research, Department of New Materials and Biosystems & University of Heidelberg, Department of Biophysical Chemistry.
‡ Carl Zeiss AG, Technology Center, Jena.
§ Carl Zeiss AG, Technology Center, Oberkochen.

selectivity between acrylic and aromatic polymer components is used to influence the surface topography. Structure depths between 8 and 30 nm have been reported in silicon, too thin to obtain a substantial antireflective effect. An alternative route to antireflective materials is offered by randomly deposited nanosized clusters and subsequent dry etching. Stochastic distributed arrays of nanotips have been realized on crystalline silicon wafers that showed remarkable antireflective properties over a broad spectral region.[23] This approach, however, does not allow for controlling of structural parameters like the diameter and the spacing period of the ARS, which is in contrast to our method.

The overall reflectance is a function of the AR-layer thickness d and the wavelength λ.[24] For a graded-index transition, substantial antireflection is obtained if the ratio d/λ is about 0.4 or higher.[10,18] Thus, for optimum antireflection conditions in the DUV region, the height of the structure should be at least 100 nm, which is a factor of 2 more than has been processed on fused silica so far. In general, the smoother the transition of the refractive index is realized, the less reflection of light is observed. Ideally, this is obtained by the fabrication of hollow, pillar-like protuberances pointing from the optical interface.

We used block copolymer micelle nanolithography (BCML)[25–27] in order to create a hexagonal mask of gold nanoparticles by a simple dipping procedure. Polystyrene-*block*-poly(2)-vinylpyridine, PS-*b*-P2VP (Mn(PS) = 190000, M_n(PVP) = 55000, M_w/M_n = 1.10, Polymersource, Inc.) diblock copolymers were dissolved in toluene with a concentration of 3 mg/mL, forming uniform spherical micelles. Tetrachloroaurate (HAuCl$_4$, Sigma Aldrich) was added to the solution with a stoichiometric loading parameter defined as $L = n[\text{Me}]/n[\text{P2VP}]$ (Me = metal salt), in order to neutralize the P2VP polymer block, which mainly represents the micellar core. After stirring for 24 h, all metal salt was dissolved. The substrates were immersed into the micellar solution and retracted with a speed of 12 mm/min. The polymer shell was removed by subsequent hydrogen plasma treatment of the samples with a TePla 100-E microwave plasma system (30 min, 0.4 mbar, and 150 W). Dip-coating has a substantial advantage over other methods because it enables a fast and homogeneous coating of plane and curved substrates. For example lenses or microlens arrays of several square centimeters can be coated within minutes with high accuracy and reproducibility. A schematic of the sample processing is described in Figure 1a.

Atomic force microscopy (AFM) measurements were performed to characterize the particle mask (Figure 1b). The spacing period was set to 110 ± 7 nm in order to be sufficiently small to avoid light interference effects in the wavelength range of interest. The particle diameter was 7 ± 1 nm and as such small enough not to introduce substantial scattering of light. The method is applicable for various kinds of materials and was used to generate nanopattern on glass, silica, quartz, calcium fluoride, mica, as well as sapphire and diamond.[25,28] In case of DUV applications, the number of suitable materials is virtually limited to fused silica, quartz, magnesium fluoride, and calcium fluoride.[2] Thus, we used
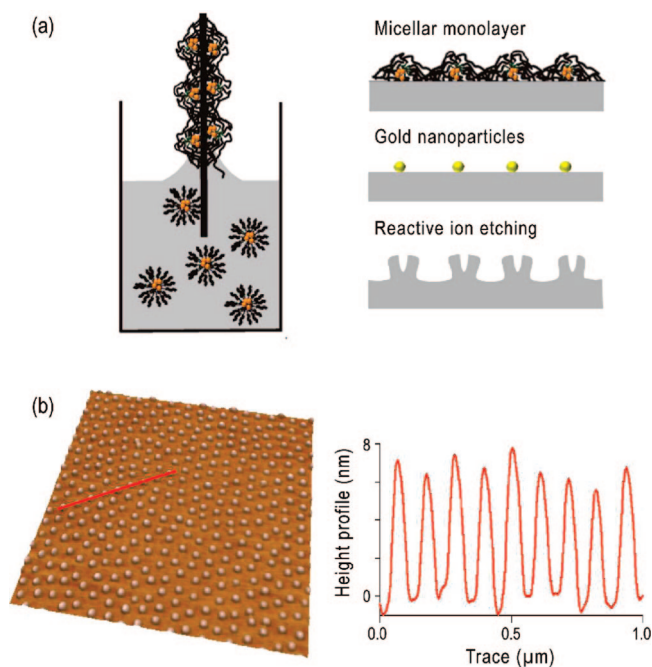

Figure 1. Schematic of the fabrication process. (a) The substrate is immersed into a toluene solution of metal salt loaded micelles. During retraction, a micellar monolayer self-assembles on top of the substrate driven by capillary forces due to the evaporation of the solvent. The polymer matrix is removed entirely by hydrogen plasma treatment and results in the deposition of an extended array of elemental gold particles on top of the substrate. Gold nanoparticles act as an efficient mask for etching hollow conelike pillars into the underlying silica support by reactive ion etching (RIE). (b) AFM image and profile of the gold particle mask. The particle spacing was measured to be 110 ± 7 nm with an average particle diameter of 7 ± 1 nm indicated by the corresponding line scan. (Scan size: 2μm × 2μm).

fused silica for our experiments, which is also the most common material for optical components.

The samples were subject to further RIE processing. As shown in Figure 2, hollow, pillar-like protuberances are etched into the substrate with a lateral pattern periodicity as set by the BCML.

Reactive ion etching was performed using a 2:3 mixture of Ar and CF$_4$ as process gas at a total flow rate of 50 sccm, pressure 40 mTorr. The RF power was set to 300 W, which induced a self-bias on the sample of 395 V. Etching time was set to 4 min. During the process, the temperature was kept constant at 20 °C. Remarkably, the pillars are hollow cones with the cone's tip reaching down to approximately half of the pillar height while the particles are removed completely (Figure 2d,f). Holes are formed at the location where the gold was originally located. This can be explained by the electrostatic sheath that is formed above the sample during the plasma process.[29] In the sheath region, a strong electric field is generated perpendicular to the surface. The presence of metallic and as such electrical conductive gold clusters on top of the insulating material, however, causes a substantial sheath distortion in the vicinity of the conductor/insulator interface (Figure 2e).[30] The reactive ions of the plasma are thereby focused to the contact area of the metallic nanoparticles with the underlying fused silica substrate. This
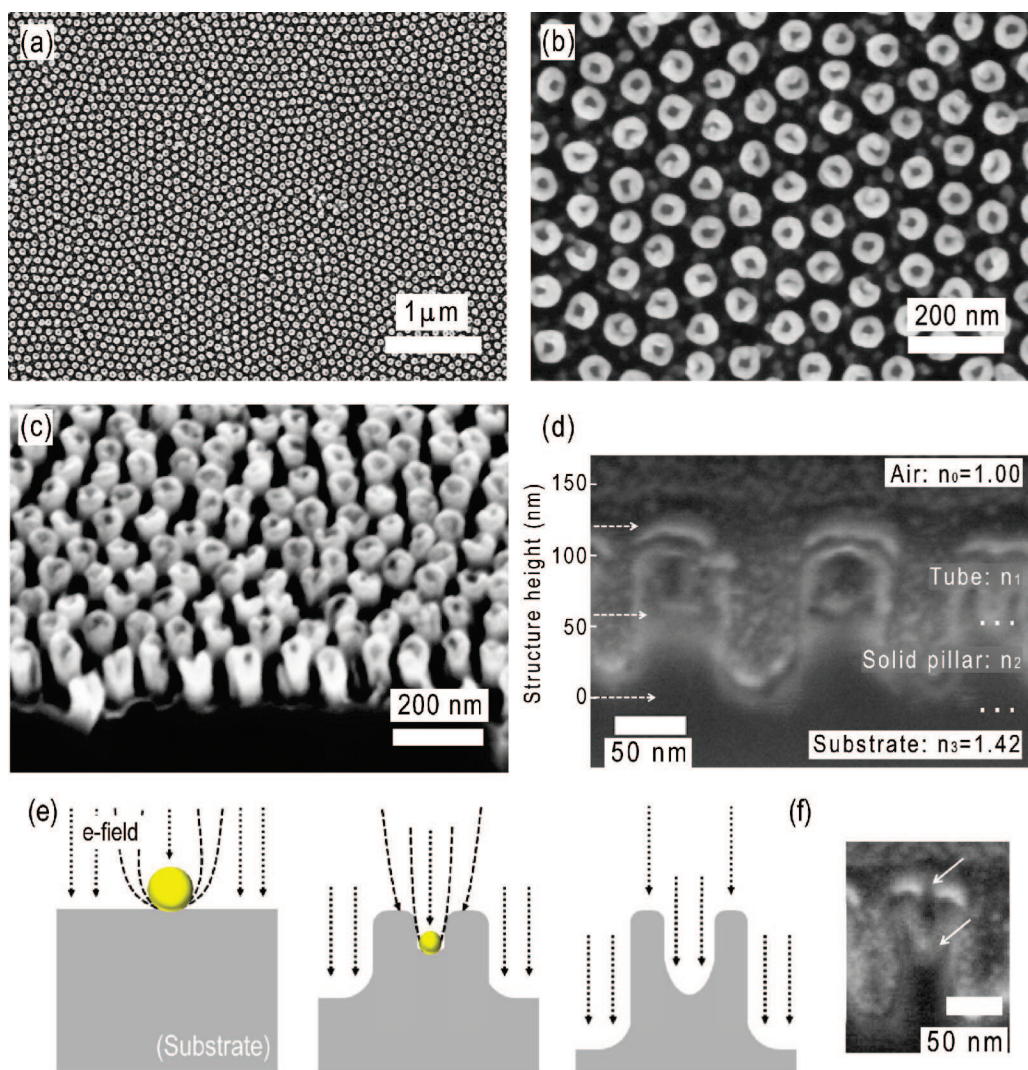
Figure 2. (a,b) Top-view SE-micrographs of the fabricated ARS displaying a quasihexagonal arrangement. (c) Side-view image of the pillar array, tilt angle of 45°. The pillars have a diameter of 60 ± 4 nm and a lateral spacing of 110 ± 7 nm (center to center), respectively. (d) Focused ion beam (FIB) cross section through the ARS displaying the refractive index gradient along the optical interface. The height of the structure was measured to be 116 ± 8 nm, which corresponds to the effective thickness of the ARS layer. A cone-type hole is etched into each pillar tip to half of the pillar height as indicated by the scale bar. The height of the hollow part of the structure was measured to be 55 ± 5 nm. (e) The schematic displays the fabrication of hollow conelike pillars during the reactive ion etching process in the presence of gold nanoparticles. (f) Close-up micrograph of a half-hollow pillar obtained as schematically described. The porous pillar tip and the bottom of the tube are indicated by white arrows. No residual nanoparticles were found inside the tubes, verifying that the gold mask is completely removed during the RIE process.

causes a strong depletion of the plasma-generated reactive ion concentration around the metal islands and enhanced etching activity below the nanoparticles. Gold itself is rather resistant against the reactive ions. During the etching, the particles sink into the material and the particle diameter continuously decreases until they are completely used off. Thus, the particles act as an etching mask for processing hollow, conelike pillars oriented perpendicular to the substrate. The outer diameter of the pillars is thereby much larger than the diameter of the nanoparticles due to the depletion of ion concentration. At the same time, the inner diameter of the hollow structure reflects the particle size.

For the substrate's antireflection properties, the gradual change of the refractive index from air to bulk is essential. The optical quality of the fused silica surface is a consequence of the strength of the gradual increase of silica mass

perpendicular to the air/substrate interface. In the present case, this is realized by a stepwise increase of the material density from air to silica tubes and solid silica pillars, finally merging into bulk silica. The different sections are resulting in a subdivided distribution of refractive index across the antireflective structure as displayed in Figure 2d,f. Consequently, the partly hollow pillars are of special importance for the antireflective quality of the optical interface.

The particle diameter as described above was found to give the best results within the RIE process. Smaller particles (<5 nm) resulted in a minor structural aspect ratio and less hollow pillars. In contrast, larger particles (≫10 nm) resulted in a smaller gap between the protuberances and broader pillar rims. At the same time, complete removal of residual gold from such larger particles was more difficult. A possible explanation is that the particles are decomposing during the
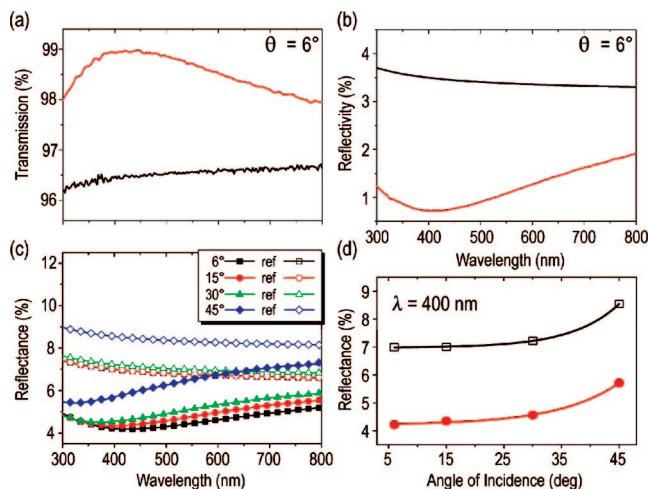
Figure 3. Broadband antireflective properties with varying incidence angles. (a,b) Wavelength-dependent transmission and reflectivity of an AR-structured fused silica sample (red line) compared to a reference (black line). The increase in transmission corresponds to an equivalent decrease in reflection. The reflectance of the sample back side was subtracted for both spectra. (c) Wavelength and angle-dependent reflectance of ARS (closed symbols) and plane fused silica (open symbols, calculated). (d) Reflectance from an ARS (red line) and a reference (black line) sample as a function of incident angle.

plasma treatment and residual gold is resputtered at the inside of the tube walls. Gold dispositions are visible by a lower transmission of the sample around 520 nm due to light absorbance of the metal, resulting in a deterioration of the optical performance.

Nature's suggestions for reducing reflection and as such to increase the transmission of light is given by the surface of a moth eye lens, which is also nanostructured with similar dimensions as shown in this report.[10] The optical performance of the ARS presented here was investigated by wavelength and angle-dependent transmission and reflection measurements. As shown in Figure 3, the reflectivity of light was decreased while transmission increased at the same time.

Transmission and reflection measurements of plane fused silica samples were performed using a Lamba 900 spectrometer (Perkin-Elmer) (for incidence angles <15°) and an ellipsometer (J. A. Woollam Vase) (for incidence angles >15°). A plane sample was measured in each case as reference. The reference measurement was also used to subtract the reflex contribution from the unstructured back side of the sample. An increase of the total transmission was observed over a spectral range from 300 to 800 nm (Figure 3a). At $\lambda = 400$ nm, the transmittance reached a maximum value of 99.0%, while the reflectivity of the same sample was damped to 0.7%. Because the improved transmission is in accordance with a reduced reflectance, it is apparent that light scattering defects or absorption losses, which might have been introduced by the fabrication process, play, if at all existing, a minor role. As already mentioned, AR-structured surfaces are advantageous over AR-layer coatings because the reflection is reduced for omnidirectional incidence of light. Ellipsometry measurements were performed to investigate the nonpolarized spectral reflection ($(R_s + R_p)/$
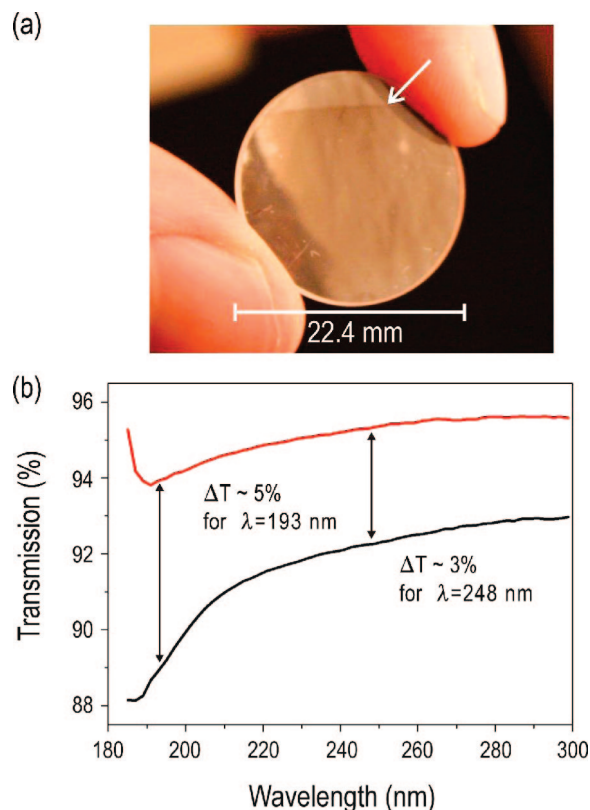

Figure 4. Optical properties of an antireflective structured lens. (a) Photograph of the processed lens demonstrating the antireflective effect. The borderline between the structured (bottom) and unstructured (top) area is indicated by the white arrow. (b) Transmission spectra of the same lens before (black line) and after (red line) processing. An increase of transmission was observed for the DUV range from 185 to 300 nm. The improved transmission values for the excimer laser wavelengths 193 nm (ArF) and 248 nm (KrF) are shown to be exemplary.

2) for different angles of incidence (Figure 3c). The reflectance data were compared with calculations of the reflectance of light from nonstructured fused quartz interfaces. The reflectivity of the subwavelength structured interface was reduced to about 3% over the whole spectral region for incidence angles up to 45°. This is also shown for a single wavelength in Figure 3d, where the reflectance is plotted as a function of the incidence angle.

To demonstrate the excellent applicability of the method to nonplanar optical components and the antireflective properties in the DUV range, the convex side of a fused silica lens was processed and characterized by sub-300 nm transmission measurements. The planconvex lens had a diameter of 22.4 mm and a focal distance of 100 mm, which corresponds to a radius of curvature of 50 mm. The reduced reflectivity in the visible light region of the structured part of the lens surface is shown in Figure 4a. More intense light reflectivity is seen above the line indicated by the white arrow, which is the borderline between the nanostructured and the unstructured part of the lens surface, whereas, the antireflective part of the lens appears less bright.

Transmission in the DUV range was measured between 185 and 300 nm using a BSM 300 spectrophotometer (SMT Oberkochen) (Figure 4b). The transmission was improved

over the whole DUV spectral region with a factor of 5% for 193 nm and 3% for 248 nm at the excimer laser wavelengths of ArF and KrF, respectively. The high increases of transmission of about 5% for $\lambda = 193$ nm relates to a virtual elimination of reflection at the modified optical interface.

In summary, a new approach for the low-cost fabrication of antireflective structured materials is demonstrated by utilizing the advantage of self-assembly based nanolithography and reactive ion etching. Quasihexagonal arrays of gold nanoparticles are used as an etching mask for plasma processing of fused silica wafers. Hollow protuberances, i.e., tubelike pillars with a structural period of 110 ± 7 nm and a height of 116 ± 8 nm, were fabricated into the optical interface. The antireflective properties of this structure were demonstrated by transmission and reflection measurements for wavelengths ranging from deep UV to IR at oblique angles of incidence. The applicability of the fabrication method has been demonstrated for planconvex fused silica lenses with the result of a substantially increased transmittance of light in the DUV region between 185 and 300 nm. Beside the remarkable optical properties, these structures offer additional advantages compared to thin-film coatings in terms of mechanical stability and durability because they are essentially free of mechanical adhesion problems and tensile stress. The method represents a fast, inexpensive, and very reproducible way for the fabrication of highly light-transmissive, antireflective optical materials to be used for display panels, projection optics, as well as heat-generating microscopic and excimer laser applications.

References

(1) Kikuta, H.; Toyota, H.; Yu, W. *Opt. Rev.* **2003**, *10* (2), 63–73.
(2) Ullmann, J.; Mertin, M.; Lauth, H.; Bernitzki, H.; Mann, K.; Ristau, D.; Arens, W.; Thielsch, R.; Kaiser, N. *Proc. SPIE* **2000**, *3902*, 514–527.
(3) Xi, J. Q.; Schubert, M. F.; Kim, J. K.; Schuber, E. F.; Chen, M.; Shawn-Yu, L.; Liu, W.; Smart, J. A. *Nat. Photonics* **2007**, *1*, 176–179.
(4) Walheim, S.; Schaeffer, E.; Mlynek, J.; Steiner, U. *Science* **1999**, *283*, 520–522.
(5) Sandrock, M.; Wiggins, M.; Shrik, J. S.; Tai, H.; Ranade, A.; Baer, E.; Hiltner, A. *Appl. Phys. Lett.* **2004**, *84* (18), 3621–3623.
(6) Dobrowolski, J. A.; Poitras, D.; Ma, P.; Vakil, H.; Acree, M. *Appl. Opt.* **2002**, *41* (16), 3075–3083.
(7) Southwell, W. H. *J. Opt. Soc. Am. A* **1991**, *8* (3), 549–553.
(8) Stavenga, D. G.; Foletti, S.; Palasantzas, G.; Arikawa, K. *Proc. Biol. Sci.* **2006**, *273* (1587), 661–667.
(9) Bernhard, C. G. *Endeavour* **1967**, *26*, 79–84.
(10) Clapham, P. B.; Hutley, M. C. *Nature* **1973**, *244* (3), 281–282.
(11) Thomas, I. M. *Appl. Opt.* **1992**, *34*, 6145–6149.
(12) Ibn-Elhaj, M.; Schadt, M. *Nature* **2001**, *410* (6830), 796–799.
(13) Kanamori, Y.; Sasaki, M.; Hane, K. *Opt. Lett.* **1999**, *24*, 1422–1424.
(14) Toyota, H.; Takahara, K.; Okano, M.; Yotsuya, T.; Kikuta, H. *Jpn. J. Appl. Phys.* **2001**, *40*, 747–749.
(15) Kanamori, Y.; Kikuta, H.; Hane, K. *Jpn. J. Appl. Phys., Part 1* **2000**, *39*, L735−L737.
(16) Motamedi, M. E.; Southwell, W. H.; Gunning, W. J. *Appl. Opt.* **1993**, *31* (22), 4371–4376.
(17) Gombert, A.; Rose, K.; Heinzel, A.; Horbelt, W.; Zanke, C.; Bläsi, B.; Wittwer, V. *Sol. Energy Mater. Sol. Cells* **1998**, *54*, 333–342.
(18) Wilson, S. J.; Hutley, M. C. *Opt. Acta* **1982**, *7*, 993–1009.
(19) Kanamori, Y.; Hane, K.; Sa, H.; Yugami, H. *Appl. Phys. Lett.* **2001**, *78* (2), 142–143.
(20) Cao, L.; Massey, J. A.; Winnik, M. A.; Manners, I.; Riethmuller, S.; Banhart, F.; Spatz, J. P.; Moller, M. *Adv. Funct. Mater.* **2003**, *13*, 271–276.
(21) Park, M.; Harrison, C.; Chaikin, P. M.; Register, R. A.; Adamson, D. H. *Science* **1997**, *276*, 1401–1404.
(22) Asakawa, K.; Hiraoka, T. *Jpn. J. Appl. Phys., Part 1* **2002**, *41*, 6112–6118.
(23) Huang, Y.-F.; Chattopadhyay, S.; Jen, Y.-J.; Peng, C.-Y.; Liu, T.-A.; Hsu, Y.-K.; Pan, C.-L.; Lo, H.-C.; Hsu, C.-H.; Chang, Y.-H.; Lee, C.-S.; Chen, K.-H.; Chen, L.-C. *Nat. Nanotechnol.* **2007**, *2*, 770–774.
(24) Rayleigh, J. S. *Proc. London Math. Soc.* **1880**, *11*, 51–56.
(25) Glass, R.; Moeller, M.; Spatz, J. P. *Nanotechnology* **2003**, *14*, 1153–1160.
(26) Glass, R.; Arnold, M.; Bluemmel, J.; Kueller, A.; Moeller, M.; Spatz, J. P. *Adv. Funct. Mater.* **2003**, *13*, 569–575.
(27) Spatz, J. P.; Sheiko, S.; Moeller, M. *Macromolecules* **1996**, *29*, 3220–3226.
(28) Spatz, J. P.; Moessmer, S.; Hartmann, C.; Moeller, M.; Herzog, T.; Krieger, M.; Boyen, H.-G.; Ziemann, P.; Kabius, B. *Langmuir* **2000**, *16*, 407–415.
(29) Langmuir, I. *Science* **1923**, *58* (1502), 290–291.
(30) Kim, D.; Economou, D. J. *J. Appl. Phys.* **2004**, *95* (7), 3311–3318.

NL080330Y